

1
2
3
4 **Sub-nm Pt Clusters on Defective NiFe LDH Nanosheets as**
5
6
7 **Trifunctional Electrocatalysts for Water Splitting and**
8
9
10 **Rechargeable Hybrid Sodium-air Battery**
11
12
13
14

15 Xueqing Yu^a, Junpo Guo^a, Bo Li^a, Jincheng Xu^a, Peng Gao^{b,*}, Kwan San Hui^c, Kwun
16
17 Nam Hui^{a,*}, Huaiyu Shao^{a,*}
18
19
20

21 ^a Joint Key Laboratory of the Ministry of Education, Institute of Applied Physics and
22
23 Materials Engineering, University of Macau, Avenida da Universidade, Taipa, Macau
24
25 SAR, China. Email: hshao@um.edu.mo, bizhui@um.edu.mo
26
27

28 ^b School of Chemistry and Molecular BioScience, University of Wollongong, NSW
29
30 2500, Australia. Email: pg177@uowmail.edu.au
31
32

33 ^c School of Engineering, Faculty of Science, University of East Anglia, Norwich, NR4
34
35 7TJ, United Kingdom
36
37
38
39
40
41
42
43
44
45
46
47
48
49
50
51
52
53
54
55
56
57
58
59
60

Abstract

It is challenging to develop highly-efficient and stable multifunctional electrocatalysts for improving hydrogen evolution reaction (HER), oxygen evolution reaction (OER), and oxygen reduction reaction (ORR) for sustainable energy conversion and storage systems such as water-alkali-electrolysers (WAEs) and hybrid sodium-air batteries (HSABs). In this work, high monodisperse sub-nm Pt clusters (NCs) on defective NiFe layered double hydroxides nanosheets (Ni_xFe LDHs) are synthesized by a facile electrodeposition method. Due to the synergistic effect between homogeneous Pt NCs and abundant atomic M(II) defects, along with hierarchical porous nanostructures, the Pt/ Ni_xFe LDHs catalysts exhibit superior trifunctional electrocatalytic activity and durability toward HER/OER/ORR. A WAE fabricated with Pt/ Ni_xFe LDHs electrodes needs 1.47 V to reach a current density of 10 mA cm^{-2} , much lower than that of the mixed 20% Pt/C and 20% Ir/C catalysts. An HSAB assembled by Pt/ Ni_xFe LDHs as a binder-free air cathode displays high open-circuit voltage, narrow overpotential gap, and remarkable rechargeability. This work provides a feasible strategy for constructing free-standing efficient trifunctional electrocatalysts for sustainable energy conversion and storage systems.

Keywords

sub-nm Pt, layered double hydroxide, cation vacancies, water splitting, hybrid Na-air Battery

1. INTRODUCTION

The advancements of green and sustainable energy conversion and storage devices, such as metal-air batteries, water-alkali-electrolyzers (WAEs), and fuel cells, are crucial for addressing issues of the energy crisis, environmental pollution, and greenhouse emissions.¹⁻³ The intrinsic sluggish kinetics and large overpotential of the half-reactions, including hydrogen evolution reaction (HER) and oxygen evolution reaction (OER) for water splitting systems, OER and oxygen reduction reaction (ORR) for metal-air batteries, greatly reduce the energy efficiency and hamper their large-scale industrialization.^{4, 5} Currently, noble metal-based catalysts are recognized as state-of-the-art catalysts for these reactions.⁶ However, Pt/C is the best known HER and ORR electrocatalyst, but a poor OER catalyst. Similarly, Ir/C and RuO₂ possess excellent catalytic activity for OER but not for HER/ORR.⁷ Therefore, it is highly desirable to develop high performance and multifunctional electrocatalysts for WAEs and metal-air batteries.

Previous studies have revealed that NiFe layered double hydroxides (NiFe LDHs) exhibit impressive OER activities in alkaline conditions due to their unique layered structure with large surface areas, which could provide abundant active sites with tunable adsorption strength of intermediates during OER.⁸⁻¹⁰ Nevertheless, the performance of NiFe LDHs is still far from satisfactory because of their poor electrical conductivity and sluggish HER/ORR electrocatalytic kinetics.¹⁰ Recent evidence suggests that the generation of cation vacancies into NiFe LDHs nanosheets is an effective route to optimize surface electronic and chemical features, improving their electronic conductivity and electrocatalytic activity.^{11, 12} Platinum (Pt) is generally considered as the unrivaled electrocatalyst for HER, but the catalytic activity in the alkaline environment is about two orders of magnitude lower than that in acidic electrolytes.^{13, 14} Pioneering works have proved that the integration of Pt into metal hydroxides is a plausible way to enhance the HER activity of Pt in basic media.¹⁴ Among various transition metal hydroxides, NiFe LDHs exhibit considerable potential as supports to immobilize Pt due to the strong synergetic interactions between Pt and site-specific supports.^{8, 15-17} Notwithstanding the superior properties of Pt-based catalysts, the high cost, scarcity, and poor durability significantly limit their universal application.⁷ Therefore, how to reduce the material cost while maintaining high catalytic performance has been a hot research topic in recent decades.¹⁸ One economical strategy is alloyed Pt with transition metals catalysts, thus the electrocatalytic performance can be enhanced through the ensemble and ligand effects.¹⁸ For example, our team has successfully fabricated PtNi bimetallic structure on NiFe LDH surface by a multi-step method, which displaying excellent bifunctional catalytic activity toward OER/ORR in basic conditions.¹⁷ It was widely accepted that Ni atoms are easily

1
2
3
4
5
6
7
8
9
10
11
12
13
14
15
16
17
18
19
20
21
22
23
24
25
26
27
28
29
30
31
32
33
34
35
36
37
38
39
40
41
42
43
44
45
46
47
48
49
50
51
52
53
54
55
56
57
58
59
60

corroded in the electrocatalytic ORR reaction, hence the alloy structure cannot maintain good durability in the long-term hybrid sodium-air battery (HSAB) rechargeability testing.^{17, 18} Another effective approach is to increase the atom utilization efficiency by reducing the particle size, thereby providing more active sites and improving specific activity.¹⁹ Unfortunately, Pt nanoparticles tend to spontaneously agglomerate and coagulate caused by their high surface energy, some capping/stabilizing agents including organic ligands, polymers, and surfactants are usually utilized to prevent the aggregation.²⁰ However, the presence of capping agents on Pt nanoparticles surface inevitably limits the accessibility of active sites and decreases their catalytic activity toward HER. Moreover, the addition of the capping agent also requires complicated and energy-consuming procedures.²¹ Thus, a feasible strategy needs to be developed to control the growth of Pt NCs on NiFe LDHs surfaces without the use of any capping agent, while retaining the high electrocatalytic activity for HER/OER. That is challenging.

Herein, a facile electrochemical deposition strategy with subsequent strong basic etching processes was proposed to prepare uniform ultrafine sub-nm Pt clusters anchored on defect-rich NiFe LDHs (Pt/Ni_xFe LDHs) *in-situ* grew on three-dimension (3D) Ni foam support. The self-standing designed structure for Pt/Ni_xFe LDHs electrodes demonstrated remarkable catalytic activity and stability towards HER/OER/ORR in alkaline media. The density functional theory (DFT) calculations showed that the introduction of base-soluble Zn(II) vacancies efficiently alters the surface electronic structure around the active sites and facilitates the adsorption of HER and OER processes intermediates. A WAE fabricated with binder-free Pt/Ni_xFe LDHs electrodes displays lower overpotentials than that of the mixed noble-metal benchmark catalysts. The binder-free Pt/Ni_xFe LDHs electrode also shows high ORR activity with a high half-wave potential. Besides, an HSAB assembled using the Pt/Ni_xFe LDHs as a binder-free cathode electrode delivers high open voltage, high round trip efficiency, and remarkable cycling durability. This study proposes a feasible and easy extendable electrochemical deposition strategy to prepare binder-free, high-performance electrodes for sustainable energy conversion and storage applications, providing new solutions to address many of the major energy and environmental challenges in other fields.

2. RESULTS AND DISCUSSION

2.1. Characterizations of Pt/Ni_xFe LDHs catalyst.

The fabrication process of the Pt/Ni_xFe LDHs catalyst was schematically illustrated in Figure 1a, where the 3D Ni foam substrate (Figure S1a and b) was

immersed into the electrolyte containing Ni, Fe, Zn, and Pt precursor. Briefly, Pt/NiZnFe LDHs were electrodeposited on the surface of Ni foam under a constant potential at room temperature. Then, the as-synthesized Pt/NiZnFe LDHs were selectively etched of basic-soluble Zn elements by strong alkaline solution treatment to manufacture M(II) vacancies, leading to form ultrafine Pt NCs decorated on defect-rich NiFe LDHs nanosheets (Pt/Ni_xFe LDHs).

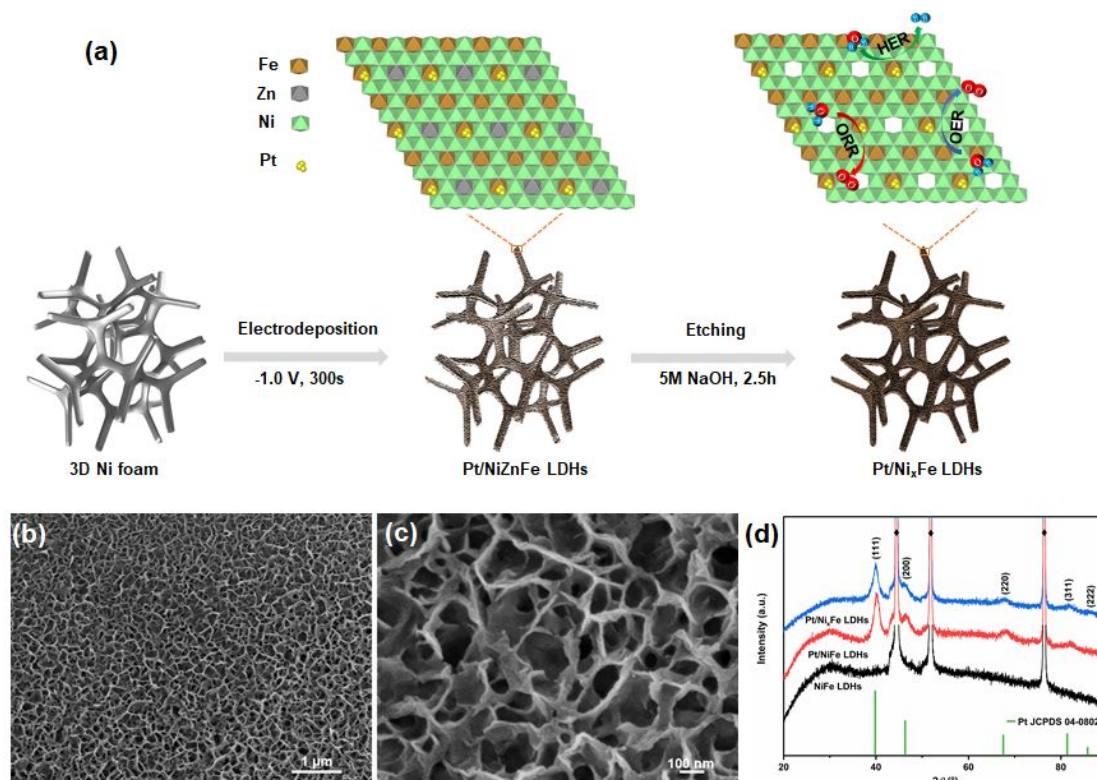


Figure 1. (a) Schematic illustration of the formation of Pt/Ni_xFe LDHs. (b, c) SEM images of Pt/Ni_xFe LDHs obtained at different magnifications. (d) XRD patterns of Pt/Ni_xFe LDHs, Pt/NiFe LDHs, and NiFe LDHs (The peaks marked “♦” stand for the Ni foam substrate.)

Scanning electron microscopy (SEM) images at different magnifications (Figure 1b, c), showed that Pt/Ni_xFe LDHs nanosheets were assembled vertically on the entire Ni skeletons, with a lateral dimension of 50 to 200 nm and thicknesses of around 10 nm. The electrodeposited Pt/Ni_xFe LDHs displayed a hierarchical porous structure with interconnected nanosheets, thus providing plenty of exposed active sites and enhancing the diffusion of ions and the generated gas. The morphology of Pt NCs was not observed due to the small particle size, which would be characterized by transmission electron microscopy (TEM) in the following section. By tuning the composite of the metal precursor, the NiFe LDHs and Pt/NiFe LDHs were also obtained with similar nanosheets morphology and orientation (Figure S1c-f). Intriguingly, we found that the shape of basic-treated Pt/Ni_xFe LDHs nanosheets became clearer and thinner than

Pt/NiZnFe LDHs (Figure S1g, h), which can be explained by the dissolution of Zn sites accompanied by the removal of OH groups, the defective laminates tended to be more positively charged leading increased intercalated anions (CO_3^{2-}) to enter the interlaminar, thus reducing the interlaminar distance.²² Figure 1d gave the X-ray diffraction (XRD) patterns of Pt/Ni_xFe LDHs, Pt/NiFe LDHs, NiFe LDHs samples on the Ni foam. Five characteristic XRD peaks centred at 40.0°, 46.4°, 67.5°, 80.2° and 85.7° which can be assigned to (111), (200), (220), (311), and (222) diffractions of the face-centered cubic (*fcc*) Pt crystal structure (JCPDS 04-0802), respectively,²³ whereas the diffraction peaks for NiFe LDHs were not detected due to their amorphous feature.²⁴ Moreover, the XRD of Pt/Ni_xFe LDHs after strong alkali etching could well keep the host structure of NiFe LDHs.

High angle annular dark-field scanning transmission electron microscopy (HAADF-STEM) images revealed that the wrinkled and ultrathin feature structure of as-synthesized Pt/Ni_xFe LDHs nanosheets (Figure 2a, b). High magnification HAADF-STEM and TEM images indicated that uniformly dispersed ultrafine Pt NCs on defect-rich NiFe LDHs nanosheets surface with a narrow particle-size distribution (Figure 2c-f). Notably, TEM images showed that nanosheets treated with strong alkaline had a negligible change in the size distribution of Pt NCs except for the thinner nanosheets structure, compared to the pristine Pt/NiZnFe LDHs (Figure S2a-c). Surprisingly, the etched Pt/Ni_xFe LDHs displayed a hierarchically micro-mesoporous structure, which not only facilitated diffusion of reactants but also increased the density of active sites with high accessibility. Previous research found that the atomic-scale distribution of Fe³⁺ cations in NiFe-LDH nanosheets played a key role in immobilizing the $[\text{PtCl}_6]^{2-}$ ions at via Fe³⁺-O(H)-Pt bonds, then formed sub-2 nm Pt NCs *in-situ* by the following electrochemical reduction in the absence of capping reagents.^{8, 16} The high-resolution TEM (HRTEM) illustrated that lattice fringes were coherently extended the entire nanoparticle, confirmed the formation of a single-crystal structure (Figure 2e), which was consistent with the selected area electron diffraction (SAED) pattern (inset of Figure 2c). The lattice spacing of 0.226 nm corresponded to the (111) planes of *fcc* Pt,²⁰ which was consistent with the XRD investigation. The HAADF-STM image and the corresponding EDS mappings were shown that the homogenous distribution of Ni, Fe, Pt, and O elements throughout the whole structure (Figure S2d). The inductively coupled plasma-mass spectrometry (ICP-MS) analysis manifested the loading amount of Pt in the optimized Pt/Ni_xFe LDHs was 2.24 wt% (Table S1). Furthermore, XPS quantitative analysis (Table S2) displayed that the surface atomic concentration of Pt in Pt/Ni_xFe LDHs approximately to 0.38 at%. Compared to the pristine NiFe LDHs, the decrease of surface oxygen atom content in Pt/Ni_xFe LDHs matrix ascribed to the removal of OH groups coordinated with Zn(OH)_x⁻ sites during the basic etching

process.²² These results fully confirmed the successful deposition of Pt on Ni_xFe LDHs nanosheets.

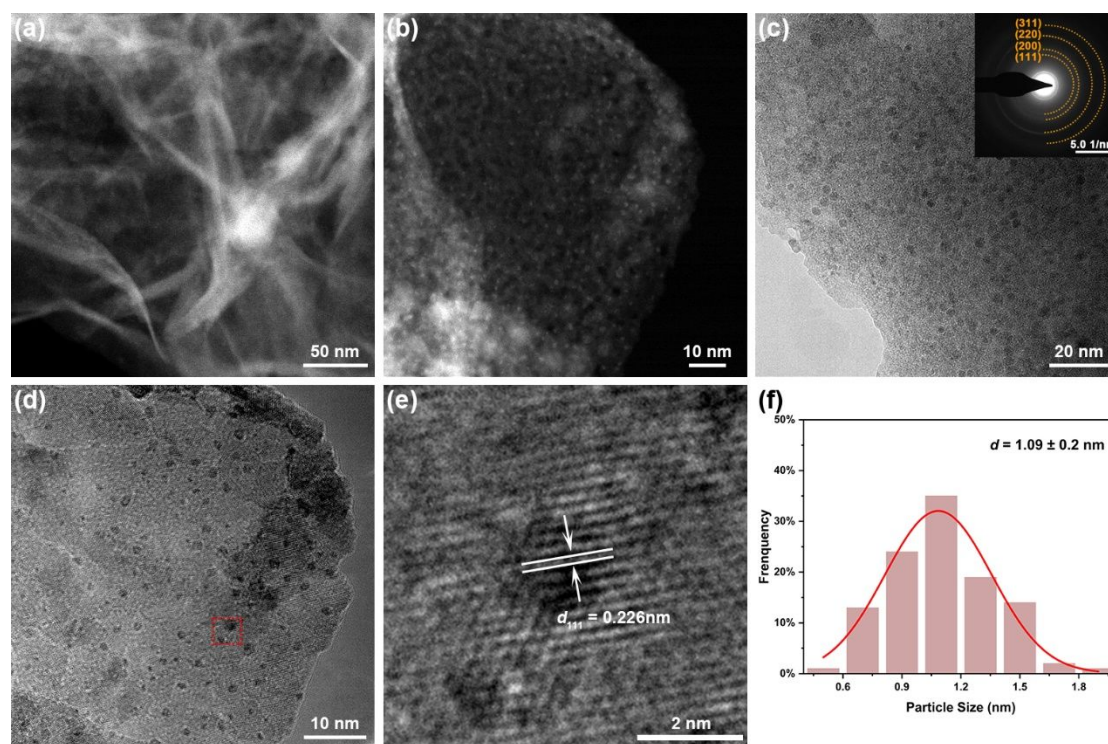


Figure 2. (a-c) HAADF-STEM, (d) TEM, (e) HRTEM images, (f) particle size distribution of deposited Pt NCs of Pt/Ni_xFe LDHs. The inset in (c) displays the corresponding SAED pattern.

The formation process of Pt/Ni_xFe LDHs nanosheets was further studied by controlling the deposition time. Irregularly bumped nanoparticles were observed on the surface of Ni foam in the early electro-synthesis process (100s, Figure S3a). With a prolonged time of 200s, the bumped subunits were grown bigger and denser, initially forming porous nanosheet-like structures (Figure S3b). As the electrodeposition increased to 300s, the hierarchical porous of LDHs nanosheets uniformly and densely coated the Ni foam skeleton (Figure S3c). While the LDHs nanosheets became larger and Pt NCs on the surface began aggregating with the extension of the reaction time (Figure S3D, e). Moreover, Pt/Ni_xFe LDHs obtained with different electrodeposition temperatures, potential, and basic-treated time were also explored. When the deposition temperature was reduced to 0°C, the reduction metal precursor and growth rate of crystal became slow, and only small nanosheets were obtained (Figure S3f). Besides, the deposition potential was a key factor affecting the final morphology of products. The good interleaved nanosheets appeared as the deposition potential increased to -1.0 V, while became accumulation and even compaction with the continued increase of the deposition potential (Figure S4). We also investigated the effect of alkali treatment time on Pt/Ni_xFe LDHs, it can be seen that the nanosheets became thinner due to the removal

of Zn(OH)_x -sites, and the layered structure remained unchanged after 2.5 h (Figure S5)²². In the present synthetic system, the morphology and contents of Pt NCs in $\text{Pt/Ni}_x\text{Fe}$ LDHs could be selectively synthesized by controlling the addition of the Pt precursor in the initial electrolyte. TEM images in Figure S6a revealed that few sparse nanoparticles were formed when reduced Pt precursor contents. While the uniform distribution of Pt NCs was obtained and began to aggregate with the increasing of precursor content (Figure S6b, c). The corresponding ICP-MS results showed that with the contents of Pt precursor increasing from 1.0 to 2.0 and 3.0 mM, the deposition amount of Pt gradually increased from 1.27 to 2.24 and 3.85 wt% (Table S1). Such facile control of the morphology and loading density of Pt NCs on Ni_xFe LDHs was quite important for tuning their electrocatalytic properties.

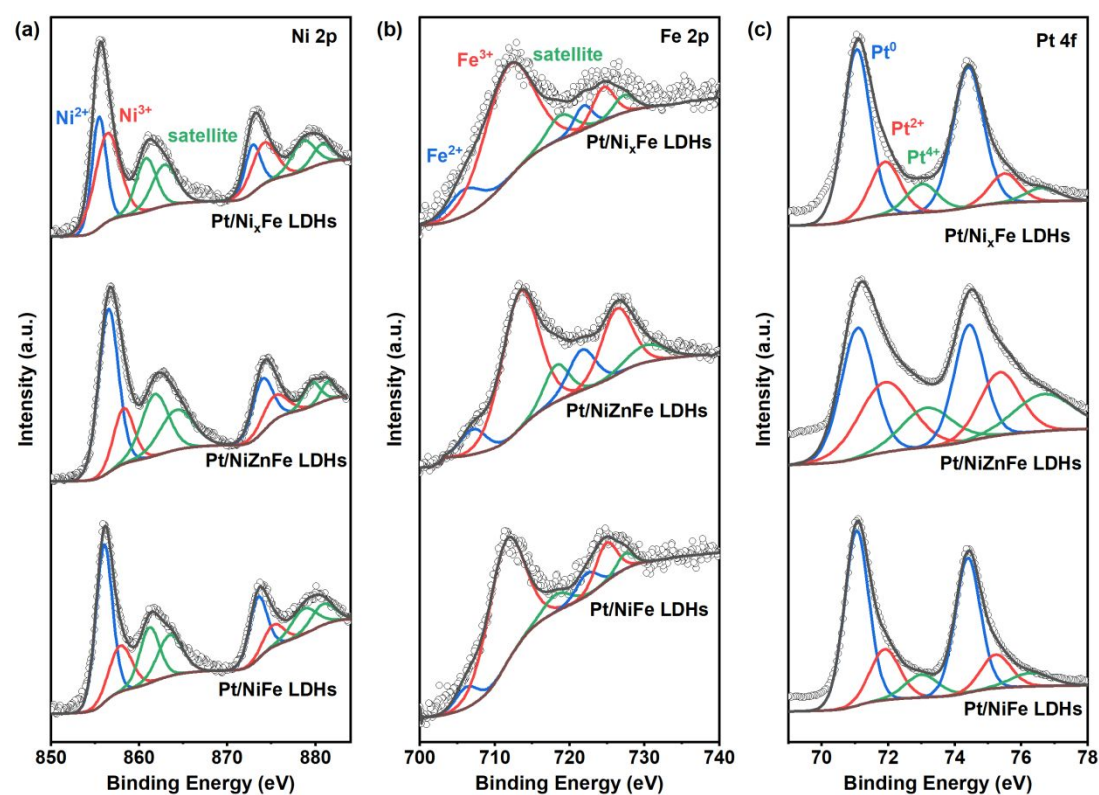


Figure 3. High resolution XPS spectra (a) Ni 2p, (b) Fe 2p and (c) Pt 4f in $\text{Pt/Ni}_x\text{Fe}$ LDHs, Pt/NiZnFe LDHs and Pt/NiFe LDHs.

X-ray photoelectron spectroscopy (XPS) was further employed to identify the chemical environment difference of the catalysts. All the XPS spectrums revealed the presence of Ni, Fe, and Pt in the as-prepared samples, while the significantly reduced of Zn 2p peaks in the defective $\text{Pt/Ni}_x\text{Fe}$ LDHs and Ni_xFe LDHs further confirmed the selective etching of Zn elements by the strong basic solution (Figure S7a and S8a). Theoretically, the surrounding unsaturated metal sites can be exposed by the basic leaching of Zn(OH)_x octahedrons from the LDHs matrix, leading to form Ni-O-Ni

1
2
3 defects,²² which were schematically shown in Figure 1a. Therefore, the valence states
4 of the metal sites surrounding the atomic defects would be changed to balance the
5 charge. As shown in Figure 3a and S8b, the Ni 2p signals of the Pt/Ni_xFe LDHs and
6 Ni_xFe LDHs were negatively shift compared with pristine Pt/NiFe LDHs and NiFe
7 LDHs, evidenced the valence states change of Ni elements. It was well accepted that
8 the Ni 2p region can be deconvoluted into Ni²⁺ and Ni³⁺ coordinated to OH located at
9 low binding energies, and their corresponding satellite peaks in the high binding
10 energies.⁴ According to the previously reported results, the high-resolution Ni 2p
11 spectrum for Pt/Ni_xFe LDHs and Ni_xFe LDHs displayed a strong Ni³⁺ ions signal with
12 a percentage of 37.1% and 37.2%, higher than those of Pt/NiFe LDHs (17.92%) and
13 NiFe LDHs (19.7%), respectively, indicating the formation of Ni²⁺ defects on the
14 surface of Pt/Ni_xFe LDHs and Ni_xFe LDHs.²⁶ The appeared Ni²⁺ defects favoured to
15 change the local chemical coordination and the surface electronic structure, finally
16 promoted the chemical valences increasing from Ni²⁺ to Ni³⁺.¹² The following DFT
17 calculations proved that the introduction of cation vacancies in the LDHs surface can
18 facilitate electron transfer and strengthen the absorption of HER and OER intermediates,
19 thus further enhancing the electrocatalytic activity in the water-splitting process. These
20 findings also resonated well with the previously reported studies.^{12, 22, 27} No obvious
21 changes of Fe 2p spectra were observed in the as-prepared samples (Figure 3b and S8c),
22 suggesting that the valence state of Fe kept unchanged after the basic dissolving of Zn
23 sites. Two dominant peaks at around 712 and 725 eV belonged to Fe 2p_{3/2} and Fe 2p_{1/2}
24 peaks, respectively, which were in agreement with the presence of Fe³⁺ in LDHs
25 materials.²⁸ The Pt 4f spectrum in Figure 3c was divided into asymmetric doublet peaks
26 located at 71.06 and 74.42 eV could be assigned to the Pt4f_{7/2} and Pt 4f_{5/2} binding
27 energies of Pt⁰, respectively, indicating the dominance of zero-valent Pt in the obtained
28 Pt/Ni_xFe LDHs sample, which was coincided with the HRTEM observation.²⁰ The O
29 1s spectrum in the electrocatalysts can be decomposed into three different oxygen
30 environments peaks, including M-O bonds, M(II)-OH and M(II)-OH functionalities
31 (Figure S7b, S8d), respectively, which was consistent well with the earlier reported
32 LDHs materials.¹⁵ The negative shift of O1s spectra in the defective Pt/Ni_xFe LDHs
33 and Ni_xFe LDHs further identifying the electronic structure disturbed around the atomic
34 defects (Ni-O-Ni).⁴ Figure S7c offered the Raman spectra of Pt/Ni_xFe LDHs, the peaks
35 at 478.1 cm⁻¹ and 547.8 cm⁻¹ were attributed to M-O-M and M-O (M=Ni²⁺, Fe³⁺)
36 vibrations, respectively, while the broad peak appeared at 685 cm⁻¹ corresponded to the
37 intercalated CO₃²⁻, further confirmed the incorporation of LDHs matrix into the nano
38 framework.²⁹

2.2. HER, OER and WAEs performance.

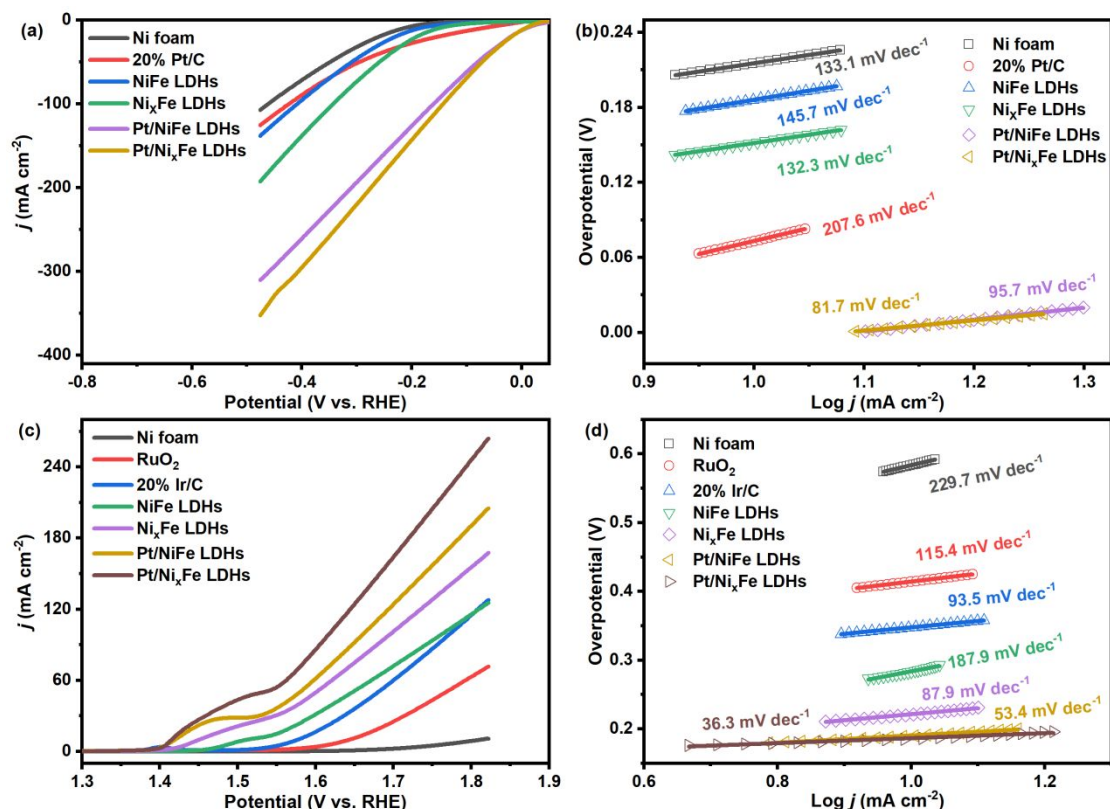


Figure 4. Polarization curves and the corresponding Tafel plots for (a, b) HER and (c, d) OER of Pt/Ni_xFe LDHs, Pt/NiFe LDHs, Ni_xFe LDHs, NiFe LDHs, commercial 20% Pt/C, RuO₂ and 20% Ir/C catalysts in 1M KOH solution.

The electrocatalytic performance toward HER and OER in 1 M KOH electrolyte was evaluated using a typical three-electrode configuration, and the as-prepared samples coated Ni foam was directly used as the working electrode. As shown in Figure 4a and S9a, the linear sweep voltammetry (LSV) curves for HER on Pt/Ni_xFe LDHs electrode exhibited significantly lower overpotential at different current densities, compared to that of bare Ni foam, NiFe LDHs, Ni_xFe LDHs, Pt/NiFe LDHs and commercial 20% Pt/C. The corresponding Tafel slopes of Pt/Ni_xFe LDHs (81.7 mV dec⁻¹) was plotted in Figure 4b, smaller than Ni foam (133.1 mV dec⁻¹), NiFe LDHs (145.7 mV dec⁻¹), Ni_xFe LDHs (132.3 mV dec⁻¹), Pt/NiFe LDHs (95.7 mV dec⁻¹) and commercial 20% Pt/C (207.6 mV dec⁻¹). Based on the former researches, the calculated Tafel slope value of the Pt/Ni_xFe LDHs catalyst indicated that the HER process follows the Volmer-Heyrovsky mechanism, where electrochemical desorption of H intermediates adsorbed (H_{ad}) was regarded as the rate-limiting step.³⁰ These results suggested that the decoration of Pt NCs efficiently improved the electrocatalytic HER activities of NiFe LDHs in alkaline media, and the induction of atomic M(II) vacancies accelerated the reaction kinetics. The superior catalytic HER performance of Pt/Ni_xFe

LDHs compared favourably with recently reported LDHs-based electrocatalysts (Table S3, Supporting Information). In addition, the stability of Pt/Ni_xFe LDHs catalyst was further explored. The LSV curves were almost unchanged after 5000 consecutive cyclic voltammograms (CV) cycles (Figure S9b) and the current density of Pt/Ni_xFe LDHs remained nearly stable during the long-term testing. The above findings demonstrated that the high catalytic activity, excellent durability, and mechanical robustness of Pt/Ni_xFe LDHs electrode for HER.

The catalytic activities of different catalysts for OER in the same electrolyte were also assessed. As displayed in Figure 4c, the LSV catalytic current density of Pt/Ni_xFe LDHs electrodes was significantly enhanced, exceeding that of Pt/NiFe LDHs, Ni_xFe LDHs, NiFe LDHs, Ni foam, benchmark RuO₂, and 20% Ir/C electrodes. Meanwhile, the Pt/Ni_xFe LDHs electrodes also delivered the significantly smaller Tafel slope of 36.3 mV dec⁻¹ (Figure 4d), as well as the lowest overpotential under different current densities (Figure S9c). The enhanced OER performance might be ascribed to the synergic effects between M(II) defects with anchored Pt NCs on the NiFe LDHs surface. By alkaline etching of Zn in Pt/NiZnFe LDHs nanosheets, the surface electronic configuration of Ni²⁺ ($t_{2g}^6e_g^0$) became adjusted and redistributed, leading form more Ni³⁺ with an optimal orbital distribution ($t_{2g}^6e_g^1$). The filling of e_g orbital increased the covalency of transition metal-oxygen bonds and promoted the absorption of oxygen reaction intermediates via stronger σ -bonding orbital overlap, and thus facilitated electron transfer and strengthen the absorption of OER intermediates (*O), further enhancing the electrocatalytic activity for OER.^{12, 31} The high electrocatalytic activity was superior to the recently reported transition metal oxides-based catalyst (Table S3). Moreover, the stability of the Pt/Ni_xFe LDHs catalyst was investigated by multi-step chronopotentiometric responses. As shown in Figure S9d, with the current density increased from 10 to 200 mA cm⁻², the polarization potential increased immediately and then levels off to remain constant for the rest 3600 s for each step. Unexpectedly, the lower potential value (1.50 vs. 1.51 V_{initial}) was established at the same current density during the reverse process, which might be attributed to the residual trace Zn in the nanocomposites dissolved by long-term immersion of basic electrolyte, the ICP-MS results showed the weight percentage of Zn decreased from 0.64% to 0.21%, hence deriving more Ni³⁺ active sites to absorb O* and decreasing the OER electrocatalytic overpotential.²⁷

To understand the extraordinary performance for both OER and HER, the electrochemical active surface areas (ECSA) of Pt/Ni_xFe LDHs, Pt/NiFe LDHs Ni_xFe LDHs, and NiFe LDHs electrode were estimated by measuring their double-layer capacitances (C_{dl}) using cyclic voltammetry in the non-Faradaic region. (Figure S10).¹⁵ The calculated ECSA value of Pt/Ni_xFe LDHs electrode was 364.7 cm², markedly

higher than those of Pt/NiFe LDHs (280.4 cm^{-2}), Ni_xFe LDHs (133.7 cm^{-2}), and NiFe LDHs (54.3 cm^{-2}), signifying the generation of M(II) atomic vacancies provides abundant active sites that are beneficial to the enhancement of electrocatalytic activity. Furthermore, the intrinsic catalytic activity toward HER and ORR was evaluated by calculating the TOF values.⁴ Obviously, Pt/Ni_xFe LDHs electrode presented consistently higher TOF values over Pt/NiFe LDHs, Ni_xFe LDHs, and NiFe LDHs electrodes for HER and OER, respectively (Figure S11). This striking increase of TOF highlighted its bifunctional electrocatalytic promising for high-performance water splitting systems. The electrochemical impedance spectroscopy (EIS) tests were performed to evaluate the reaction kinetics during the HER and OER processes. The corresponding Nyquist plots and fitted results of the as-prepared catalysts were shown in Figure 5 and Table S4. The Electrolyte resistance (R_s) of 1M KOH electrolyte in the fabricated electrochemical test system was about 1.3Ω . Compared with the Ni foam (74.80 and 9.82Ω), NiFe LDHs (38.03 and 3.36Ω) and Pt/NiFe LDHs (0.63 and 0.92

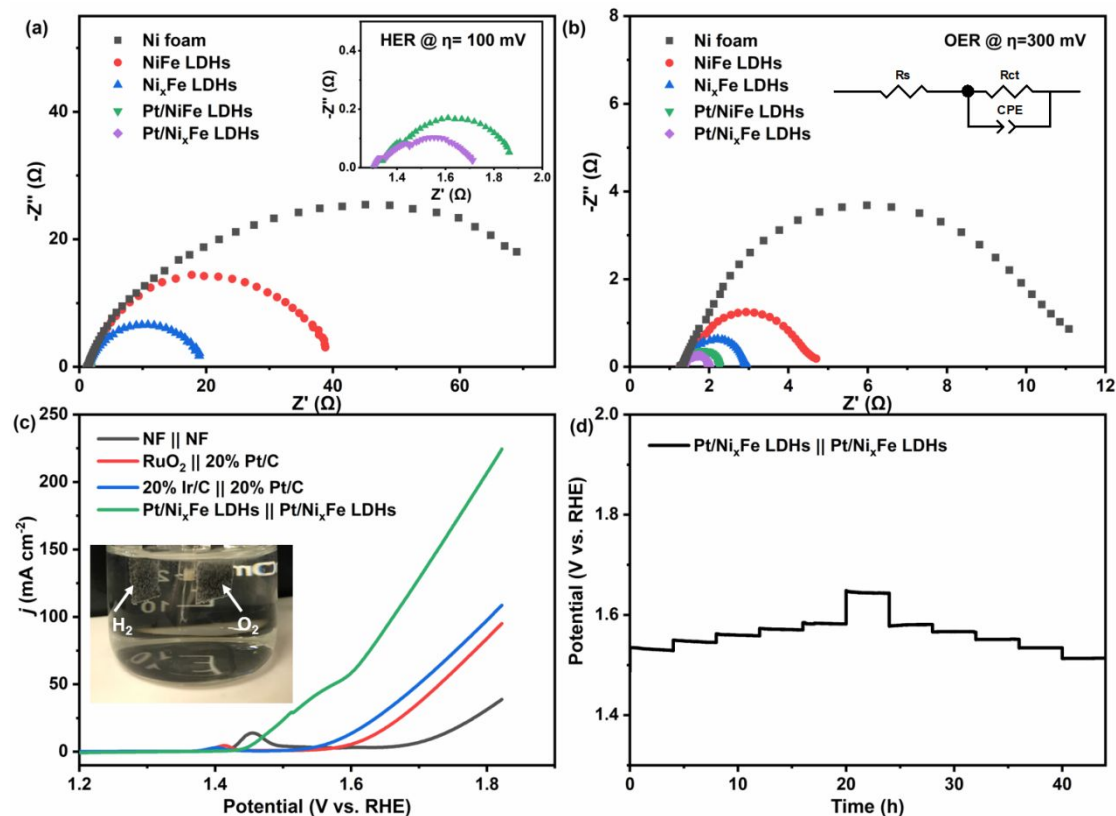


Figure 5. The Nyquist plots and corresponding equivalent electric circuit model of Ni foam, NiFe LDHs, Ni_xFe LDHs, Pt/NiFe LDHs, and Pt/Ni_xFe LDHs electrodes for (a) HER and (b) OER at an overpotential of 100 and 300 mV, respectively, in 1 M KOH solution. (c) Polarization curves for overall water splitting system and the inset optical image of O₂ and H₂ generated on Pt/Ni_xFe LDHs || Pt/Ni_xFe LDHs, RuO₂ || 20% Pt/C, 20% Ir/C || 20% Pt/C and NF || NF as both anode and cathode, respectively. (d) Multi-current process of Pt/Ni_xFe LDHs electrodes. The current density started at 10 increased to 20, 30, 40, 50, and 100, then down to 50, 40, 30, 20, and 10 mA cm⁻² every 4 h.

1
2
3
4 Ω), the defective Ni_xFe LDHs (17.93 and 1.63 Ω) and Pt/ Ni_xFe LDHs (0.46 and 0.64
5 Ω) electrodes showed smaller charge transfer resistance (R_{ct}), suggesting superior
6 electron conductivity and faster charge transfer kinetics in both HER and OER process.
7
8 Meanwhile, the smallest R_{ct} value of Pt/ Ni_xFe LDHs electrode demonstrating the
9 enhanced reaction kinetics after tethering Pt NCs on Ni_xFe LDHs surface. These results
10 further revealed that the introduction of Pt clusters and the manufacture of defective
11 M(II) sites promoted electron transfer and ion diffusion in the electrocatalytic process.
12
13

14 The crystal structure and chemical properties of Pt/ Ni_xFe LDHs electrode after
15 long-term durability tests were further tracked by XRD, XPS, SEM, and TEM
16 techniques. Although the accelerated degradation tests (ADTs) for HER, OER, and
17 ORR might cause considerable damage to the nanosheets, the overall phase structure
18 and elemental composition of Pt/ Ni_xFe LDHs were retained after the long-term ADT
19 tests (Figure S12a and b).³² For the HER stability test, no obvious changes in Ni 2p
20 were observed before and after 5000 CVs cycles and the percentage of Ni^{3+} remained
21 at 37.0% (Figure S12c) close to the initial value of 37.1%. Moreover, the XPS spectrum
22 of Pt 4f also maintained the metallic state Pt (Pt^0) without serious oxidation peaks in
23 the high binding energy (Figure S12d). These findings further confirmed the binder-
24 free design and hierarchical structure of Pt/ Ni_xFe LDHs electrode could effectively
25 promote the diffusion of HER intermediates to prevent the passivation of active sites,
26 thereby maintaining the excellent electrocatalytic activity and long-term durability. For
27 the OER stability analysis, as shown in Figure S12c, the content of Ni^{3+} was raised to
28 39.7% compared with an initial 37.1%, the following DFT calculations revealed the
29 increased defective sites reduce the adsorption energy of OER intermediates (Figure
30 S19), thus leading to the decreased electrocatalytic overpotential (Figure S9d). The Pt
31 4f XPS spectra exhibited a predominantly high active metallic state (Pt^0) accompanied
32 with incremental oxidation state ratios (Pt^{4+}) in high binding energy (Figure S12d),
33 which was attributed to the surface oxidation under high potential in the OER process.¹⁷
34 Similar results were observed in Pt/ Ni_xFe LDHs electrode after long-term ORR stability
35 test, the slight oxidation of Pt caused by chemisorption of surface oxygenated species
36 (Figure S12c and d).³³ This further emphasized the metallic state of Pt with high
37 catalytic activity could maintain during the process of reversible oxygen
38 electrocatalysis. Moreover, the morphology Pt/ Ni_xFe LDHs electrode after long-term
39 durability tests were also investigated. As given in Figure S13, the interconnected
40 nanosheets structure remains unchanged and Pt NCs attached on Ni_xFe LDHs
41 nanosheets without obvious detachment or aggregation, suggesting splendid
42 mechanical and electrocatalytic stability. In brief, all the data indicated the outstanding
43 catalytic activity and long-term stability of the Pt/ Ni_xFe LDHs electrode for HER, OER,
44 and ORR.
45
46
47
48
49
50
51
52
53
54
55
56
57
58
59
60

The outstanding HER and OER performances of the Pt/Ni_xFe LDHs make it a promising bifunctional electrocatalyst for overall water splitting. A WAE was built by using Pt/Ni_xFe LDHs on Ni foam as cathode and anode, respectively (Figure S14a). As shown in Figure 5c, the Pt/Ni_xFe LDHs || Pt/Ni_xFe LDHs electrolyzer yielded a current density of 10 mA cm⁻² at 1.47 V, corresponding to an overpotential of 240 mV for overall water splitting. This value was much lower than that of the commercial catalyst 20% Ir/C || 20% Pt/C (1.59 V, 360 mV), RuO₂ || 20% Pt/C (1.62 V, 390 mV) electrodes and recently reported transition metal-based bifunctional electrocatalysts for overall water splitting (Table S5). Vigorous hydrogen and oxygen bubbles were observed at both cathode and anode, respectively, during the overall water splitting process, as given in the inset photograph of Figure 5c. Moreover, the Pt/Ni_xFe LDHs || Pt/Ni_xFe LDHs couple maintained excellent stability under various current densities in a chronoamperometric test for 44 h continuous operations (Figure 5d). Upon increasing the current density from 10 to 100 mA cm⁻², the cell voltage increased accordingly and quickly became stable at each step, and delivered similar potentials change with the above OER chronoamperometric test in the reverse process. The observation was in good coincident with the enhanced OER performance caused by exposed more Ni³⁺ sites in long term alkaline soaking and further supported by the enhanced catalytic performance obtained after the stability test (Figure S14b). Additionally, the morphology of Pt/Ni_xFe LDHs kept well on both cathode and anode after the durability test (Figure S14c, d). Therefore, the Pt/Ni_xFe LDHs unfolded a high performance of overall water splitting with excellent bifunctional electrocatalytic activity and stability.

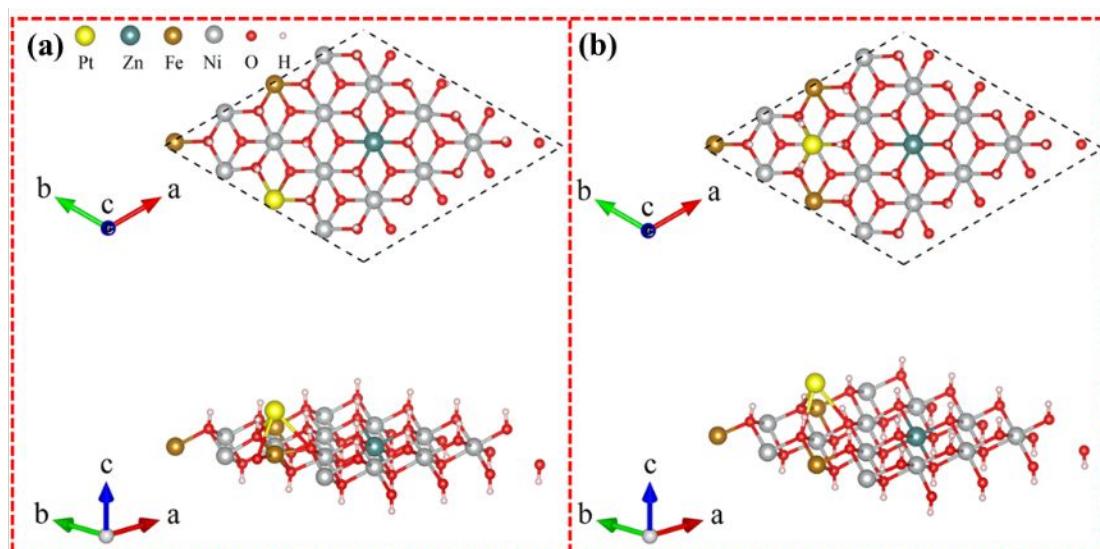


Figure 6. Atomic structure of Pt atom bonding with (a) Fe site and (b) Ni site in NiZnFe LDHs.

Several significant parameters such as deposition time, potential, temperature, base-etching time, and different metal proportions, which might influence the catalytic

1
2
3
4 activity were also investigated. By contrast, the HER catalytic activity and C_{dl} of
5 Pt/Ni_xFe LDHs initially increased along with the prolonged deposition time and
6 achieved a maximum value at 300 s (Figure S15a, b). However, the C_{dl} decreased
7 significantly with the further extending deposition time. The results exhibited that
8 excessive LDHs and Pt NCs loading would decrease the electrochemical surface area
9 and catalytic efficiency. Moreover, the HER performance and C_{dl} investigation of
10 electrochemical deposition potential (Figure S15c, d), temperature (Figure S15e, f), and
11 base-etching time (Figure S15g, h) were in good agreement with before SEM
12 morphology characterization, further verified the optimized experimental condition for
13 obtained Pt/Ni_xFe LDHs with high electrocatalytic activity and good morphology.
14
15

16
17
18 Notably, the electrocatalytic performances of Pt/Ni_xFe LDHs electrodes were
19 enhanced significantly after Fe elements incorporation into the NiZn(OH)_x lattice, as
20 shown in Figure S16. The introduction of Fe to LDHs matrix not only improved the
21 ionic conductivity and but also promoted the electrons transfer to adsorbed reactants due
22 to the highly dispersed FeO₆ octahedra.^{34, 35} Moreover, the positively charged Fe³⁺
23 in the LDH matrix also acted as stronger bonding sites to immobilize Pt NCs, which was
24 further verified by the DFT calculation (Figure 6). The adsorption energy of Pt NCs via
25 the Fe³⁺-O(H)-Pt bonding was -4.87 eV, which was lower than that of Ni²⁺-O(H)-Pt
26 bonding (-4.61 eV), suggesting the strong interaction of Pt NCs with site-specific Ni_xFe
27 LDH sheets, which was consistent with previous studies.¹⁶ Therefore, the Pt/Ni_xFe
28 LDHs electrode displayed remarkably catalytic stability compared with that absence of
29 Fe precursor (Figure S16d). The observed slopes indicated that the ECSA was increased
30 obviously after introducing a small amount of Fe elements while excessive usage led to
31 negative effects (Figure S16e), which was agreed well with the electrocatalytic
32 performance. The effects of different Ni/Zn molar ratios on the catalytic performance
33 were also investigated by maintained the usage of Fe and Pt precursor unchanged. As
34 given in Figure S17, appropriate Ni/Zn ratios in Pt/Ni_xFe LDHs matrix could decrease
35 the initial potential and overpotential, and even achieved an extremely large current
36 density under high potential. Compared with others, Pt/Ni_xFe LDHs (Ni to Zn is 9:1)
37 exhibited not only decent trifunctional catalytic properties but also enlarged ECSA
38 which can provide more active sites (Figure S17d). Moreover, in the present method,
39 the amount of Pt precursor was another key factor for the formation of high-
40 performance catalysts. Figure S18 revealed that the trifunctional catalytic properties
41 were enhanced significantly after tethering Pt NCs on the defective Ni_xFe LDHs surface.
42 The catalytic performance was linearly correlated with the addition of the Pt precursor,
43 while the ECSA was decreasing with the continuous increased usage of Pt precursor
44 (Figure S18d). This may be attributed to the high amount of Pt precursor induced the
45 aggregation of Pt NCs on the surface of Ni_xFe LDHs, as shown in Figure S6, thus
46
47
48
49
50
51
52
53
54
55
56
57
58
59
60

resulting in the decreasing of active sites and unsatisfied electrocatalytic performance. The above results further illustrated the flexibility and expansibility of the developed electrosynthesis method, as well as the controllable adjustment of the catalytic properties.

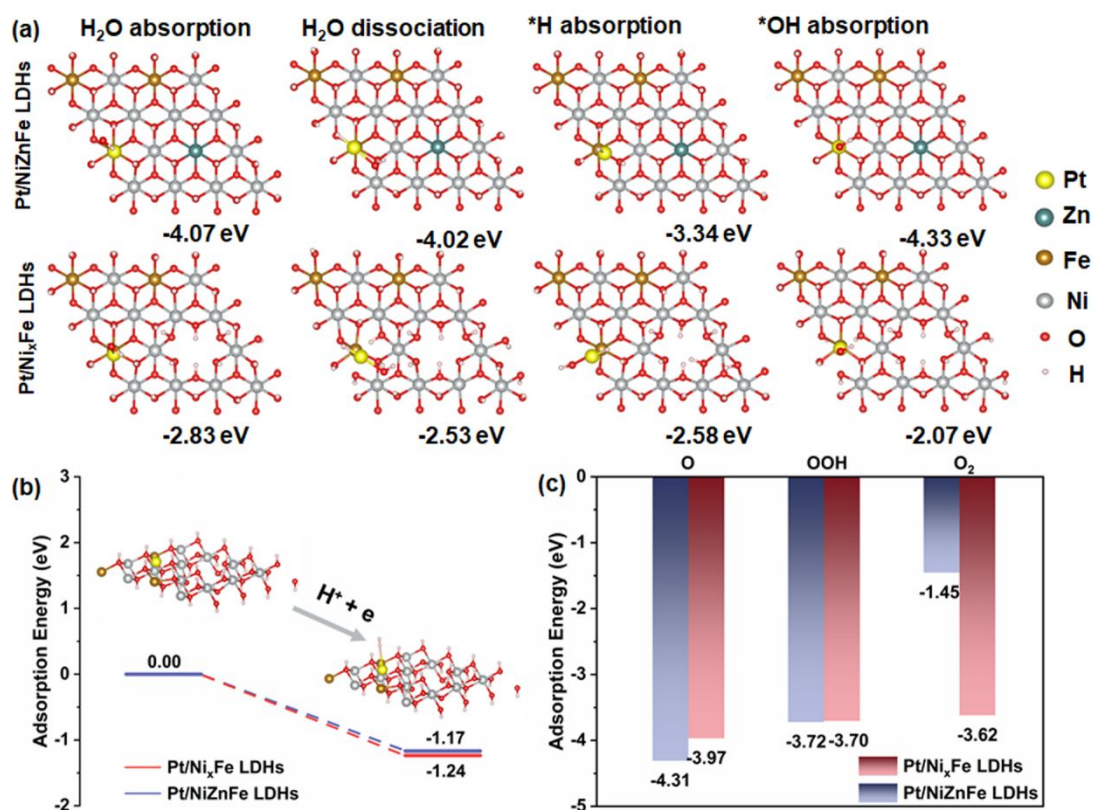


Figure 7. (a) Optimized model structures of H₂O, H₂O dissociation, *H, and *OH intermediates adsorbed on Pt/Ni_xFe LDHs and Pt/NiZnFe LDHs surfaces. (b) Calculated adsorption energy diagrams for H₂ desorption; (c) adsorption energies of *O, *OOH, and O₂ on Pt/Ni_xFe LDHs and Pt/NiZnFe LDHs surfaces.

DFT calculations were further performed to investigate the inherent relationship between the electronic structure and the outstanding electrocatalytic HER/OER performance under alkaline conditions. In this study, to better describe the interatomic interactions, in our *Ab initio* calculations, we applied Pt atom, instead of Pt nanoparticle; however, we admitted that these nanoparticles are not atomically dispersed in practical applications. As shown in Figure 7a, the defective Pt/Ni_xFe LDHs exhibited a lower water adsorption energy of -2.83 eV compared with Pt/NiZnFe LDHs, indicating an accelerated Volmer step. Based on the water-splitting reaction in alkaline media, the adsorption energy of activated H₂O, *H, and *OH intermediates were calculated on the Pt sites in NiZnFe LDHs and Ni_xFe LDHs, respectively. As given in Figure 7a, the absorption energy of intermediates on Pt/Ni_xFe LDHs was lower than that on the pristine Pt/NiZnFe LDHs, leading to more rapid H_{ad} and hydroxyl adsorption and

1
2
3 reduction/oxidation processes.³⁶⁻³⁸ Besides, Pt/Ni_xFe LDHs presented weakened
4 adsorption energy of H₂ (-1.24 eV) compared to Pt/NiZnFe LDHs (-1.17 eV),
5 demonstrating that the generated H₂ on the Pt/Ni_xFe LDHs surface were more easily
6 desorbed to avoid accumulation, thus facilitating the exposure of active sites and further
7 accelerating the reaction process (Figure 7b). Moreover, the defective Pt/Ni_xFe LDHs
8 showed a similarly enhanced OER process with a low adsorption energy of *O and
9 *OOH intermediates and superior desorption of O₂ (Figure 7c and S19). The above
10 results further verified the manufactured M(II) defects on Pt/Ni_xFe LDHs could
11 effectively decrease the electrocatalytic reaction barrier and enhance reaction kinetics
12 by adjusting the electronic structure of surrounding active sites, thereby achieving
13 highly efficient water splitting performance, which was in good agreement with our
14 experimental findings (ie. XPS, LSVs and EIS).

21 Based on the above studies, we propose the following discussions which may
22 explain the excellent electrocatalytic activity of the Pt/Ni_xFe LDHs catalyst: (1) the
23 unique layered structure of LDHs with large surface areas could provide sufficient
24 electroactive sites and stronger bonding sites to immobilize Pt NCs (via the Fe³⁺-O(H)-
25 Pt bonding). (2) the *in-situ* growth of sub-nm Pt NCs improves the electrical
26 conductivity of LDHs and accelerates the electrocatalytic kinetic process. (3) the
27 intimate contact between Pt NCs with LDHs forms profitably synergic effects, which
28 could facilitate the dissociation of H_{ad} and recombine into molecular hydrogen. (4) the
29 introduction of M(II) vacancies tunes the surface electronic structure, optimizes the
30 adsorption of O intermediates, promotes the evolution of O₂. (5) the overall hierarchical
31 porous architecture enables good mechanical adhesion, promotes fast electron/mass
32 transport and rapid gas bubble dissipation. Furthermore, the Pt/Ni_xFe LDHs catalyst
33 was directly deposited on conductive substrates to fabricate 3D freestanding electrodes
34 in the absence of binder or capping additives, enhancing the intrinsic electrocatalytic
35 activity of active sites. Thus, the above intriguing merits undoubtedly make Pt/Ni_xFe
36 LDHs a binderless, bifunctional, and high-performing catalyst in the overall
37 electrochemical water splitting system.
38
39
40
41
42
43
44
45
46
47
48
49
50
51
52
53
54
55
56
57
58
59
60

2.3. ORR and HSABs performance.

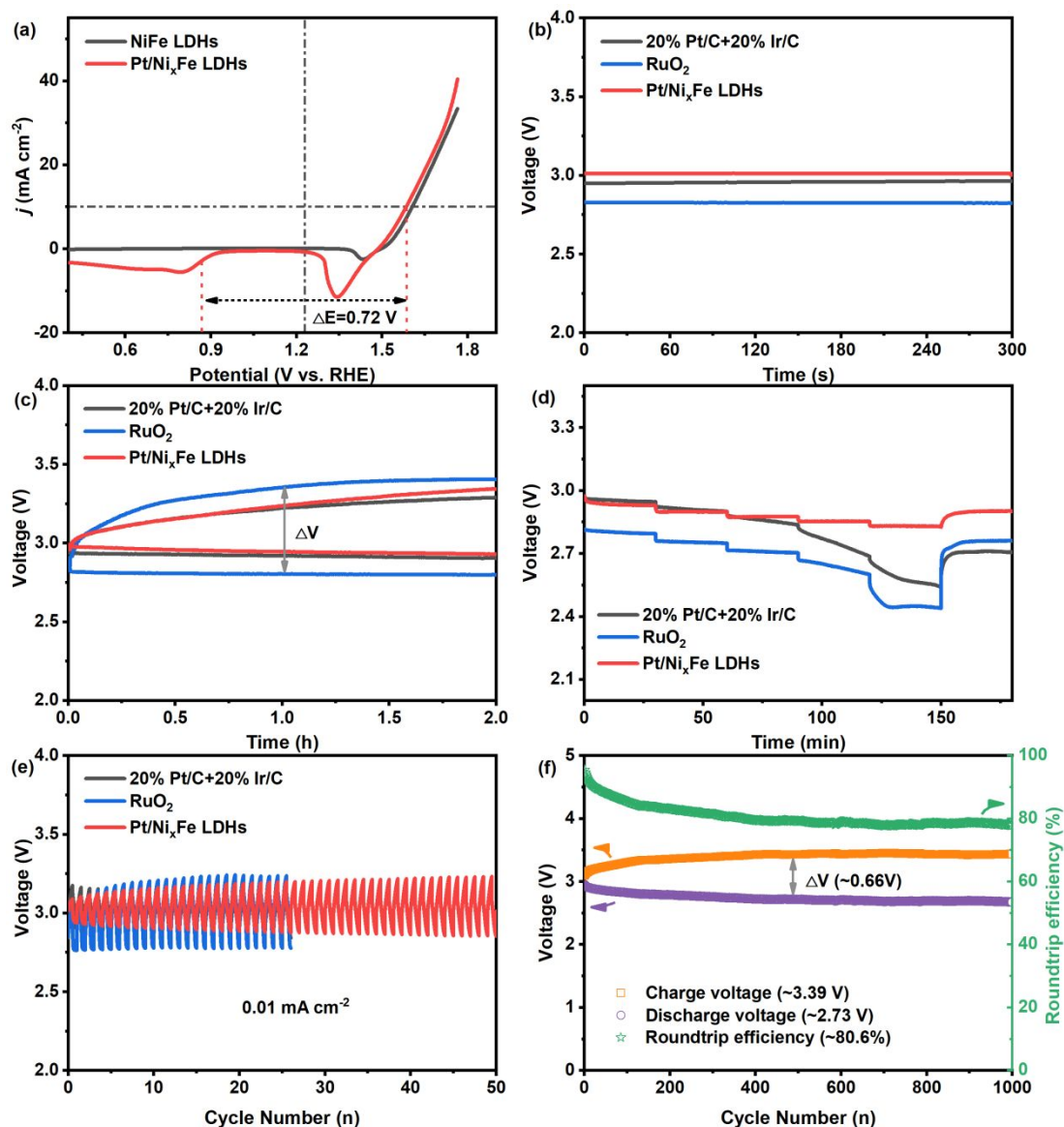


Figure 8. (a) ORR/OER bifunctional LSV curves of Pt/Ni_xFe LDHs and NiFe LDHs. (b) Open-circuit voltage plots, (c) charge-discharge voltage curves, (d) discharge voltage curves under from 0.01 increased to 0.02, 0.03, 0.04, 0.05 then reversed to 0.01 mA cm⁻² every 30 mins, and (e) cycling tests of HASBs with different electrocatalysts at air cathode. (f) The terminal voltages, overpotential gap (ΔV), and roundtrip efficiency during cycling of HSABs using Pt/Ni_xFe LDHs.

Apart from the excellent HER activity, Pt-based material was also considered as the best of ORR catalysts.³⁹⁻⁴¹ Therefore, the ORR catalytic activities of Pt/Ni_xFe LDHs were also investigated in 0.1 M O₂-saturated KOH electrolyte. As shown in Figure 8a, Pt/Ni_xFe LDHs exhibited a catalytic ORR peak with a high half-wave potential ($E_{1/2}$) of 0.87 V, while no obvious ORR signal was observed for the compared NiFe LDHs catalyst, suggesting the improved ORR activity by immobilization of Pt NCs on LDHs

1
2
3 nanosheet. The peaks around 1.3-1.4 were ascribed to the reduction of Ni^{3+} ions.²⁸ The
4 potential difference between $E_{j=10}$ (the potential required for generating a current
5 density of 10 mA cm^{-2} for OER) and $E_{1/2}$ (noted as $\Delta E = E_{j=10} - E_{1/2}$) was calculated to
6 evaluate the bifunctional catalytic activities toward OER and ORR (Figure 8a). Notably,
7 the reversible oxygen overpotential of Pt/ Ni_xFe LDHs was 0.72 V, lower than recently
8 reported bifunctional electrocatalysts (Table S6). The remarkable OER and ORR
9 bifunctional electrocatalytic activity and self-supporting features of Pt/ Ni_xFe LDHs
10 made it an appealing air electrode material for rechargeable metal-air batteries and fuel
11 cells.
12

13
14
15
16
17 As one of the promising next-generation batteries, hybrid Na-air batteries (HSABs)
18 are received considerable attention owing to their high specific capacity (838 mAh g^{-1}),
19 higher theoretical standard cell voltage (3.11 V), and low cost.^{42, 43} Strikingly, the
20 HSAB fabricated with Pt/ Ni_xFe LDHs air cathode exhibited a stable open-circuit
21 voltage of 3.01 V, which was almost near the standard voltage of 3.11 V, higher than
22 that of referential battery with 20% Pt/C+20% Ir/C (2.95 V) and RuO_2 (2.83 V) as the
23 cathode (Figure 8b), suggesting its preeminent ORR performance. It is widely known
24 that the sluggish kinetics of OER/ORR processes on the cathode side is the main reason
25 for the large voltage gap (ΔV).⁴⁴ In contrast, the battery using the Pt/ Ni_xFe LDHs
26 delivered a stable charge/discharge plateau (2.93/3.34 V) with a narrow ΔV of 0.41 V
27 and high round trip efficiency of 87.7%, suggesting the superior bifunctional OER and
28 ORR catalytic performance on air electrode (Figure 8c). Figure 8d shown the discharge
29 curves of HSABs using different air cathodes at various current densities. Compared to
30 benchmark commercial catalysts, Pt/ Ni_xFe LDHs based-HSAB exhibited relatively
31 linear and steady discharge performance, indicating good ORR performance and
32 excellent stability benefited from the freestanding electrode structure. Moreover, the
33 favourable stability of Pt/ Ni_xFe LDHs was further validated by cycling tests, no stark
34 polarization observed in the initial 50 cycles (Figure 8e), while the 20% Pt/C+20% Ir/C
35 and RuO_2 -based battery failed less than 30 cycles, indicating good rechargeability of
36 Pt/ Ni_xFe LDHs based-battery. Dramatically, the Pt/ Ni_xFe LDHs-based battery achieved
37 long-term cycling over 1000 cycles under a current density of 0.01 mA cm^{-2} with 10
38 min discharge/charge (Figure S20), corresponding with an average charge/discharge
39 voltage of $\sim 3.39/\sim 2.73 \text{ V}$, a small voltage drop of $\sim 0.66 \text{ V}$ and high round trip efficiency
40 of $\sim 80.6 \%$ (Figure 8f), significantly surpassing the previously reported HSABs (Table
41 S7). Besides, the negligible change of morphology after the long-term durability test
42 further elucidated the excellent cycling stability (inset in Figure S20).
43
44
45
46
47
48
49
50
51
52
53
54
55

56 Generally, the superior performance and remarkable rechargeability of Pt/ Ni_xFe
57 LDHs based air cathode might be ascribed to the following features: (1) the enhanced
58 kinetic synergy between M(II) vacancies and Pt NCs on nanosheet surface, which
59
60

1
2
3
4
5
6
7
8
9
10
11
12
13
14
15
16
17
18
19
20
21
22
23
24
25
26
27
28
29
30
31
32
33
34
35
36
37
38
39
40
41
42
43
44
45
46
47
48
49
50
51
52
53
54
55
56
57
58
59
60

minimizes the potential difference between OER and ORR in alkaline medium. (2) the hierarchically porous architecture enables high accessibility for electroactive sites, rapid mass transfer, and inhibits the accumulation of cycling-derived byproducts. (3) the binder-free design possesses more exposed active sites, resulting in superior electrode performance. (4) the Pt/Ni_xFe LDHs vertically grown on 3D Ni foam ensures high electroconductivity and good structure stability.

3. CONCLUSIONS

In summary, a facile, effective electrochemical deposition strategy was proposed to prepare binder-free, high-performance electrodes for HER/OER/ORR. Sub-nm Pt NCs *in-situ* decorated on defects-rich Ni_xFe LDHs nanosheets on Ni foam electrodes were prepared without using any capping reagents. M(II) vacancies in Ni_xFe LDHs nanosheets were generated from dissolving Zn sites in LDHs nanosheets, offering abundant coordinatively unsaturated active sites to absorb oxygen intermediates. The synergistic effects between abundant M(II) vacancies and sub-nm Pt NCs on LDH substrate, along with the hierarchically porous architecture, enhance the dissociation of H_{ad} and optimize the adsorption of O intermediates, which greatly promotes the overall water splitting process. Moreover, the Pt/Ni_xFe LDHs electrode shows good electrocatalytic activities with a reversible oxygen overpotential of 0.72 V in alkaline electrolytes. Using Pt/Ni_xFe LDHs as a binder-free cathode in the HSAB, it delivers a high open-circuit voltage of 3.01 V with a narrow voltage gap of 0.41 V, excellent cycling stability and rechargeability over 1000 cycles compared to the mixed commercial catalysts. It is anticipated that this facile and scalable strategy of preparation of binder-free, high-performance electrodes would provide new opportunities to exploit future multifunctional electrocatalysts for practical sustainable energy conversion and storage technologies.

4. EXPERIMENTAL SECTION

4.1. Synthesis of Pt/NiZnFe LDHs, Pt/NiFe LDHs, NiZnFe LDHs, and NiFe LDHs.

Pt/NiZnFe LDHs were prepared by a facile electrodeposition method. Typically, Ni foam (10*20*0.05 mm³) was treated with 3M HCl ultrasonicated for 15 min, then washed with water and ethanol to obtain a clean surface. The electrodeposition was conducted in a standard three-electrode system cell, well-cleaned Ni foam as the working electrode, Pt plate as the counter electrode, and Ag/AgCl (3 M KCl) as the reference electrode, respectively. The Pt/NiZnFe LDHs were synthesized in an electrolyte containing NiSO₄·6H₂O (0.027 M), ZnSO₄·7H₂O (0.003 M), FeSO₄·7H₂O (0.01 M), and K₂PtCl₆ (0.002 M). The potentiostatic deposition was carried out at -1.0

1
2
3
4 V (vs. AgCl) for 300 s at room temperature. The obtained Pt/NiZnFe LDHs was rinsed
5 carefully by water and ethanol, then left dried overnight in a vacuum oven., By
6 replacing NiSO₄·6H₂O (0.027 M) and ZnSO₄·7H₂O (0.003 M) with NiSO₄·6H₂O (0.03
7 M) obtained the Pt/NiFe LDHs. For NiZnFe LDHs, the electrolyte was prepared
8 similarly as Pt/NiZnFe LDHs except removed the Pt precursor. For NiFe LDHs, the
9 electrolyte was the same as NiFe LDHs except for Pt/NiFe LDHs except removed the
10 Pt precursor. The rest electrosynthesis process was the same as the above.
11
12
13
14

15 **4.2. Synthesis of Pt/Ni_xFe LDHs, Ni_xFe LDHs**

16
17
18 The introduction of Ni²⁺ vacancies in Pt/NiZnFe LDHs nanosheets or NiZnFe
19 LDHs has followed the reported method with slight modification.¹² Briefly, the as-
20 prepared Pt/NiZnFe LDHs or NiZnFe LDHs were treated with 5 M NaOH for 2.5 h at
21 room temperature. The obtained product was washed with water and ethanol at least
22 three times and then dried overnight. The Pt/Ni_xFe LDHs or Ni_xFe LDHs nanosheets
23 were synthesized.
24
25
26
27

28 **4.3. Electrochemical measurements**

29
30
31 Electrochemical measurements were performed with a three-electrode system
32 using a CH760E electrochemical workstation at room temperature. The obtained
33 electrocatalysts on Ni Foam (1*1 cm²) were used as the working electrode, a platinum
34 plate, and an Ag/AgCl (3M KCl) electrode was used as the counter and the reference
35 electrode, respectively. All potentials measured were calibrated versus the reversible
36 hydrogen electrode (RHE). HER and OER were investigated in 1 M KOH electrolyte,
37 while the ORR test was studied in an O₂-saturated 0.1 M KOH aqueous solution. The
38 linear sweep voltammograms (LSVs) were recorded at a scanning rate of 10 mV s⁻¹
39 without *iR* compensation. For more details see the Supporting Information.
40
41
42
43
44

45 **4.5. Assembly and test of HSABs**

46
47
48 The hybrid Na-air battery was fabricated in a sandwich structure using ceramic
49 solid electrolyte NASICON with the composition of Na₃Zr₂Si₂PO₁₂ having a high ionic
50 conductivity of 8.9 × 10⁻⁴ S cm⁻¹ at room temperature as a separator. Briefly, the anode
51 compartment was assembled in the glove box. The metallic sodium plate was first
52 placed into the chamber as the anode, followed by adding organic electrolyte (1 M
53 NaClO₄ in tetraethylene glycol dimethyl ether). NASICON solid electrolyte was
54 selected to seal the anode part to ensure that one side was in contact with the organic
55 electrolyte and the other side was exposed to air. The as-prepared air electrode was
56 directly immersed in the O₂-saturated 0.1 M NaOH electrolyte under ambient air as the
57
58
59
60

1
2
3 cathode part.

4
5 The as-prepared samples on Ni foam (diameter 10 mm) were directly used as the
6 air cathodes. By contrast, the 20% Pt/C+20% Ir/C and RuO₂ catalyst were coated on Ni
7 foam (diameter 10 mm) with the mass loading of 1 mg cm⁻², respectively.

8
9 Battery tests were performed at room temperature by LAND test station (CT2001
10 A, Wuhan LAND electronics). Cycling performance was recorded at recurrent
11 galvanostatic pulses for 5 min of discharge followed by 5 min charge.
12
13

14 15 **4.6. Theoretical Calculations**

16
17 All the calculations were conducted within Viena Ab initio Simulation Package
18 (VASP),^{45, 46} and the structure optimization was based on density functional theory
19 (DFT). The modeling of exchange-correlation energy was performed with the
20 implemented generalized gradient approximation (GGA), proposed by Perdew-Burke-
21 Ernzerhof (PBE).^{47, 48} The valence electronic states were expanded with the plane
22 waves; and the core-valence interactions were described using the projector augmented
23 wave (PAW) approach,⁴⁹ with the corresponding cutoff kinetic energies set to 450 eV.
24 For our simulated systems, the total number of atoms is larger than 160, thus the
25 Brillouin zone was set with a Gamma-centered k-point grid of 1x1x1.⁵⁰ And, to further
26 improve the convergence of the simulated systems, a Gaussian functionalized Fermi
27 surface, with a broadening magnitude of 0.1 eV was used. The structures were first
28 relaxed with the implemented conjugate-gradient algorithm, until the convergence
29 tolerance of Hellmann-Feynman forces and energy on each atom was less than 0.02
30 eV/Å and 10⁻⁴ eV/atom, respectively. Moreover, due to the periodic boundary
31 conditions (PBC), there exist non-negligible interactions among periodical images; to
32 reasonably overcome this, a separate vacuum layer, with a thickness of 15 Å along the
33 z-direction, was applied. Also, for all the calculations, spin polarization was considered.
34 Since we merely focus on the relative energies of concrete reactions rather than the
35 band gaps, we didn't introduce DFT + U corrections into our Ab initio calculations in
36 this study.
37
38
39
40
41
42
43
44
45
46
47
48

49 **ASSOCIATED CONTENT**

50 51 **Supporting Information**

52
53 The Supporting Information is available free of charge online or the author.

54
55 Characterization instruments, experimental details, SEM, TEM images, XPS analysis,
56 Raman spectra, XRD patterns, additional electrochemical test analysis, DFT
57 calculations, battery performance, ICP-MS results, and comparison with other reported
58
59
60

1
2
3 materials.
4
5

6 AUTHOR INFORMATION

7 8 Corresponding Authors

9
10 **Peng Gao** - School of Chemistry and Molecular BioScience, University of Wollongong,
11 NSW 2500, Australia. Email: pg177@uowmail.edu.au

12
13 **Kwun Nam Hui** - Joint Key Laboratory of the Ministry of Education, Institute of
14 Applied Physics and Materials Engineering, University of Macau, Avenida da
15 Universidade, Taipa, Macau SAR, China. Email: bizhui@um.edu.mo

16
17 **Huaiyu Shao** - Joint Key Laboratory of the Ministry of Education, Institute of Applied
18 Physics and Materials Engineering, University of Macau, Avenida da Universidade,
19 Taipa, Macau SAR, China. Email: hshao@um.edu.mo
20
21
22

23 Authors

24
25 **Xueqing Yu** - Joint Key Laboratory of the Ministry of Education, Institute of Applied
26 Physics and Materials Engineering, University of Macau, Avenida da Universidade,
27 Taipa, Macau SAR, China.
28

29
30 **Junpo Guo** - Joint Key Laboratory of the Ministry of Education, Institute of Applied
31 Physics and Materials Engineering, University of Macau, Avenida da Universidade,
32 Taipa, Macau SAR, China.
33

34
35 **Bo Li** - Joint Key Laboratory of the Ministry of Education, Institute of Applied Physics
36 and Materials Engineering, University of Macau, Avenida da Universidade, Taipa,
37 Macau SAR, China.
38

39
40 **Jincheng Xu** - Joint Key Laboratory of the Ministry of Education, Institute of Applied
41 Physics and Materials Engineering, University of Macau, Avenida da Universidade,
42 Taipa, Macau SAR, China.
43

44
45 **Kwan San Hui** - School of Engineering, Faculty of Science, University of East Anglia,
Norwich, NR4 7TJ, United Kingdom
46

47 Notes

48
49 There are no conflicts to declare.
50

51 ACKNOWLEDGMENTS

52
53
54 This work was funded by the Science and Technology Development Fund, Macau
55 SAR (File no. 0019/2019/AGJ, 0062/2018/A2, 0191/2017/A3, 0041/2019/A1,
56 0046/2019/AFJ) and University of Macau (File no. MYRG2019-00055-IAPME,
57 MYRG2017-00216-FST, and MYRG2018-00192-IAPME), and the UEA funding. The
58
59
60

DFT calculations were performed at High Performance Computing Cluster (HPCC) which is supported by Information and Communication Technology Office (ICTO) of the University of Macau.

REFERENCES

- (1) Wei, C.; Rao, R. R.; Peng, J.; Huang, B.; Stephens, I. E. L.; Risch, M.; Xu, Z. J.; Shao-Horn, Y. Recommended Practices and Benchmark Activity for Hydrogen and Oxygen Electrocatalysis in Water Splitting and Fuel Cells. *Adv. Mater.* **2019**, *31*, 1806296.
- (2) Sun, C.; Alonso, J. A.; Bian, J. Recent Advances in Perovskite-Type Oxides for Energy Conversion and Storage Applications. *Adv. Energy Mater.* **2020**, 2000459.
- (3) Han, J.; Bao, H.; Wang, J.-Q.; Zheng, L.; Sun, S.; Wang, Z. L.; Sun, C. 3D N-Doped Ordered Mesoporous Carbon Supported Single-Atom Fe-N-C Catalysts with Superior Performance for Oxygen Reduction Reaction and Zinc-Air Battery. *Appl. Catal. B* **2021**, *280*, 119411.
- (4) Tang, Y.; Liu, Q.; Dong, L.; Wu, H. B.; Yu, X.-Y. Activating the Hydrogen Evolution and Overall Water Splitting Performance of NiFe LDH by Cation Doping and Plasma Reduction. *Appl. Catal. B* **2020**, *266*, 118627.
- (5) Wang, H.; Fang, Q.; Gu, W.; Du, D.; Lin, Y.; Zhu, C. Noble Metal Aerogels. *ACS Appl. Mater. Interfaces* **2020**, *12*, 52234-52250.
- (6) Shi, Q.; Zhu, C.; Du, D.; Lin, Y. Robust Noble Metal-Based Electrocatalysts for Oxygen Evolution Reaction. *Chem. Soc. Rev.* **2019**, *48*, 3181-3192.
- (7) Debe, M. K. Electrocatalyst Approaches and Challenges for Automotive Fuel Cells. *Nature* **2012**, *486*, 43-51.
- (8) Han, J.; Meng, X.; Lu, L.; Wang, Z. L.; Sun, C. Triboelectric Nanogenerators Powered Electrodepositing Tri-Functional Electrocatalysts for Water Splitting and Rechargeable Zinc-Air Battery: A Case of Pt Nanoclusters on NiFe-LDH Nanosheets. *Nano Energy* **2020**, 104669.
- (9) Lee, S.; Bai, L.; Hu, X. Deciphering Iron-Dependent Activity in Oxygen Evolution Catalyzed by Nickel-Iron Layered Double Hydroxide. *Angew. Chem. Int. Ed.* **2020**, *59*, 8072-8077.
- (10) Meng, X.; Han, J.; Lu, L.; Qiu, G.; Wang, Z. L.; Sun, C. Fe²⁺-Doped Layered Double (Ni, Fe) Hydroxides as Efficient Electrocatalysts for Water Splitting and Self-Powered Electrochemical Systems. *Small* **2019**, *15*, 1902551.
- (11) Zhang, J.; Wu, X.; Cheong, W.-C.; Chen, W.; Lin, R.; Li, J.; Zheng, L.; Yan, W.; Gu, L.; Chen, C. Cation Vacancy Stabilization of Single-Atomic-Site Pt₁/Ni(OH)_x Catalyst for Diboration of Alkynes and Alkenes. *Nature Commun.* **2018**, *9*, 1-8.
- (12) Wang, Y.; Qiao, M.; Li, Y.; Wang, S. Tuning Surface Electronic Configuration

of NiFe LDHs Nanosheets by Introducing Cation Vacancies (Fe or Ni) as Highly Efficient Electrocatalysts for Oxygen Evolution Reaction. *Small* **2018**, *14*, 1800136.

(13) Subbaraman, R.; Tripkovic, D.; Strmcnik, D.; Chang, K.-C.; Uchimura, M.; Paulikas, A. P.; Stamenkovic, V.; Markovic, N. M. Enhancing Hydrogen Evolution Activity in Water Splitting by Tailoring Li⁺-Ni(OH)₂-Pt Interfaces. *Science* **2011**, *334*, 1256-1260.

(14) Yin, H.; Zhao, S.; Zhao, K.; Muqsit, A.; Tang, H.; Chang, L.; Zhao, H.; Gao, Y.; Tang, Z. Ultrathin Platinum Nanowires Grown on Single-Layered Nickel Hydroxide with High Hydrogen Evolution Activity. *Nature Commun.* **2015**, *6*, 1-8.

(15) Anantharaj, S.; Karthick, K.; Venkatesh, M.; Simha, T. V.; Salunke, A. S.; Ma, L.; Liang, H.; Kundu, S. Enhancing Electrocatalytic Total Water Splitting at Few Layer Pt-NiFe Layered Double Hydroxide Interfaces. *Nano Energy* **2017**, *39*, 30-43.

(16) Han, Y.; Li, P.; Liu, J.; Wu, S.; Ye, Y.; Tian, Z.; Liang, C. Strong Fe³⁺-O(H)-Pt Interfacial Interaction Induced Excellent Stability of Pt/NiFe-LDH/RGO Electrocatalysts. *Sci. Rep.* **2018**, *8*, 1-9.

(17) Yu, X.; Kang, Y.; Wang, S.; San Hui, K.; Hui, K. N.; Zhao, H.; Li, J.; Li, B.; Xu, J.; Chen, L. Integrating PtNi Nanoparticles on NiFe Layered Double Hydroxide Nanosheets as a Bifunctional Catalyst for Hybrid Sodium-Air Batteries. *J. Mater. Chem. A* **2020**, *8*, 16355-16365.

(18) Zhang, L.; Doyle-Davis, K.; Sun, X. Pt-Based Electrocatalysts with High Atom Utilization Efficiency: From Nanostructures to Single Atoms. *Energy Environ. Sci.* **2019**, *12*, 492-517.

(19) Shao, M.; Peles, A.; Shoemaker, K. Electrocatalysis on Platinum Nanoparticles: Particle Size Effect on Oxygen Reduction Reaction Activity. *Nano Lett.* **2011**, *11*, 3714-3719.

(20) Cheng, H.; Cao, Z.; Chen, Z.; Zhao, M.; Xie, M.; Lyu, Z.; Zhu, Z.; Chi, M.; Xia, Y. Catalytic System Based on Sub-2 nm Pt Particles and Its Extraordinary Activity and Durability for Oxygen Reduction. *Nano Lett.* **2019**, *19*, 4997-5002.

(21) Xu, H.; Ding, L.-X.; Feng, J.-X.; Li, G.-R. Pt/Ni(OH)₂-NiOOH/Pd Multi-Walled Hollow Nanorod Arrays as Superior Electrocatalysts for Formic Acid Electrooxidation. *Chem. Sci.* **2015**, *6*, 6991-6998.

(22) Xie, Q.; Cai, Z.; Li, P.; Zhou, D.; Bi, Y.; Xiong, X.; Hu, E.; Li, Y.; Kuang, Y.; Sun, X. Layered Double Hydroxides with Atomic-Scale Defects for Superior Electrocatalysis. *Nano Res.* **2018**, *11*, 4524-4534.

(23) Wang, L.; Yamauchi, Y. Block Copolymer Mediated Synthesis of Dendritic Platinum Nanoparticles. *J. Am. Chem. Soc.* **2009**, *131*, 9152-9153.

(24) Bodhankar, P. M.; Sarawade, P. B.; Singh, G.; Vinu, A.; Dhawale, D. S. Recent Advances in Highly Active Nanostructured NiFe LDH Catalyst for Electrochemical

- 1
2
3 Water Splitting. *J. Mater. Chem. A* **2021**, *9*, 3180-3208.
- 4
5 (25) Lu, X.; Zhao, C. Electrodeposition of Hierarchically Structured Three-
6 Dimensional Nickel-Iron Electrodes for Efficient Oxygen Evolution at High Current
7 Densities. *Nature Commun.* **2015**, *6*, 1-7.
- 8
9 (26) Li, P.; Duan, X.; Kuang, Y.; Li, Y.; Zhang, G.; Liu, W.; Sun, X. Tuning
10 Electronic Structure of NiFe Layered Double Hydroxides with Vanadium Doping
11 toward High Efficient Electrocatalytic Water Oxidation. *Adv. Energy Mater.* **2018**, *8*,
12 1703341.
- 13
14 (27) Liu, H.; Wang, Y.; Lu, X.; Hu, Y.; Zhu, G.; Chen, R.; Ma, L.; Zhu, H.; Tie, Z.;
15 Liu, J.; Jin, Z. The Effects of Al Substitution and Partial Dissolution on Ultrathin
16 NiFeAl Ternary Layered Double Hydroxide Nanosheets for Oxygen Evolution
17 Reaction in Alkaline Solution. *Nano Energy* **2017**, *35*, 350-357.
- 18
19 (28) Gao, Z. W.; Liu, J. Y.; Chen, X. M.; Zheng, X. L.; Mao, J.; Liu, H.; Ma, T.; Li,
20 L.; Wang, W. C.; Du, X. W. Engineering NiO/NiFe LDH Intersection to Bypass Scaling
21 Relationship for Oxygen Evolution Reaction Via Dynamic Tridimensional Adsorption
22 of Intermediates. *Adv. Mater.* **2019**, *31*, 1804769.
- 23
24 (29) Tang, C.; Wang, H. S.; Wang, H. F.; Zhang, Q.; Tian, G. L.; Nie, J. Q.; Wei, F.
25 Spatially Confined Hybridization of Nanometer-Sized NiFe Hydroxides into
26 Nitrogen-Doped Graphene Frameworks Leading to Superior Oxygen Evolution
27 Reactivity. *Adv. Mater.* **2015**, *27*, 4516-4522.
- 28
29 (30) Jaramillo, T. F.; Jørgensen, K. P.; Bonde, J.; Nielsen, J. H.; Horch, S.;
30 Chorkendorff, I. Identification of Active Edge Sites for Electrochemical H₂ Evolution
31 from MoS₂ Nanocatalysts. *Science* **2007**, *317*, 100-102.
- 32
33 (31) Suntivich, J.; May, K. J.; Gasteiger, H. A.; Goodenough, J. B.; Shao-Horn, Y.
34 A Perovskite Oxide Optimized for Oxygen Evolution Catalysis from Molecular Orbital
35 Principles. *Science* **2011**, *334*, 1383-1385.
- 36
37 (32) Yu, L.; Yang, J. F.; Guan, B. Y.; Lu, Y.; Lou, X. W. Hierarchical Hollow
38 Nanoprisms Based on Ultrathin Ni-Fe Layered Double Hydroxide Nanosheets with
39 Enhanced Electrocatalytic Activity Towards Oxygen Evolution. *Angew. Chem. Int. Ed.*
40 **2018**, *57*, 172-176.
- 41
42 (33) Tian, X.; Zhao, X.; Su, Y.-Q.; Wang, L.; Wang, H.; Dang, D.; Chi, B.; Liu, H.;
43 Hensen, E. J.; Lou, X. W. D. Engineering Bunched Pt-Ni Alloy Nanocages for Efficient
44 Oxygen Reduction in Practical Fuel Cells. *Science* **2019**, *366*, 850-856.
- 45
46 (34) Fu, Q.; Li, W.-X.; Yao, Y.; Liu, H.; Su, H.-Y.; Ma, D.; Gu, X.-K.; Chen, L.;
47 Wang, Z.; Zhang, H. Interface-Confined Ferrous Centers for Catalytic Oxidation.
48 *Science* **2010**, *328*, 1141-1144.
- 49
50 (35) Trotochaud, L.; Young, S. L.; Ranney, J. K.; Boettcher, S. W. Nickel-Iron
51 Oxyhydroxide Oxygen-Evolution Electrocatalysts: The Role of Intentional and
52
53
54
55
56
57
58
59
60

- 1
2
3
4
5
6
7
8
9
10
11
12
13
14
15
16
17
18
19
20
21
22
23
24
25
26
27
28
29
30
31
32
33
34
35
36
37
38
39
40
41
42
43
44
45
46
47
48
49
50
51
52
53
54
55
56
57
58
59
60
- Incidental Iron Incorporation. *J. Am. Chem. Soc.* **2014**, *136*, 6744-6753.
- (36) Zhang, B.; Zhu, C.; Wu, Z.; Stavitski, E.; Lui, Y. H.; Kim, T.-H.; Liu, H.; Huang, L.; Luan, X.; Zhou, L. Integrating Rh Species with NiFe-Layered Double Hydroxide for Overall Water Splitting. *Nano Lett.* **2019**, *20*, 136-144.
- (37) Chen, G.; Wang, T.; Zhang, J.; Liu, P.; Sun, H.; Zhuang, X.; Chen, M.; Feng, X. Accelerated Hydrogen Evolution Kinetics on NiFe-Layered Double Hydroxide Electrocatalysts by Tailoring Water Dissociation Active Sites. *Adv. Mater.* **2018**, *30*, 1706279.
- (38) Cai, Z.; Zhou, D.; Wang, M.; Bak, S. M.; Wu, Y.; Wu, Z.; Tian, Y.; Xiong, X.; Li, Y.; Liu, W. Introducing Fe²⁺ into Nickel-Iron Layered Double Hydroxide: Local Structure Modulated Water Oxidation Activity. *Angew. Chem. Int. Ed.* **2018**, *130*, 9536-9540.
- (39) Nie, Y.; Li, L.; Wei, Z. Recent Advancements in Pt and Pt-Free Catalysts for Oxygen Reduction Reaction. *Chem. Soc. Rev.* **2015**, *44*, 2168-2201.
- (40) Li, C.; Tan, H.; Lin, J.; Luo, X.; Wang, S.; You, J.; Kang, Y.-M.; Bando, Y.; Yamauchi, Y.; Kim, J. Emerging Pt-Based Electrocatalysts with Highly Open Nanoarchitectures for Boosting Oxygen Reduction Reaction. *Nano Today* **2018**, *21*, 91-105.
- (41) Dong, J.-C.; Zhang, X.-G.; Briega-Martos, V.; Jin, X.; Yang, J.; Chen, S.; Yang, Z.-L.; Wu, D.-Y.; Feliu, J. M.; Williams, C. T. In Situ Raman Spectroscopic Evidence for Oxygen Reduction Reaction Intermediates at Platinum Single-Crystal Surfaces. *Nature Energy* **2019**, *4*, 60-67.
- (42) Kim, J. K.; Lee, E.; Kim, H.; Johnson, C.; Cho, J.; Kim, Y. Rechargeable Seawater Battery and Its Electrochemical Mechanism. *ChemElectroChem* **2015**, *2*, 328-332.
- (43) Xu, X.; San Hui, K.; Dinh, D. A.; Hui, K. N.; Wang, H. Recent Advances in Hybrid Sodium-Air Batteries. *Mater. Horiz.* **2019**, *6*, 1306-1335.
- (44) Manikandan, P.; Kishor, K.; Han, J.; Kim, Y. Advanced Perspective on the Synchronized Bifunctional Activities of P2-Type Materials to Implement an Interconnected Voltage Profile for Seawater Batteries. *J. Mater. Chem. A* **2018**, *6*, 11012-11021.
- (45) Grimme, S. Semiempirical Gga-Type Density Functional Constructed with a Long-Range Dispersion Correction. *J Comput. Chem.* **2006**, *27*, 1787-1799.
- (46) Kresse, G.; Furthmüller, J. Efficient Iterative Schemes for Ab Initio Total-Energy Calculations Using a Plane-Wave Basis Set. *Phys. Rev. B* **1996**, *54*, 11169.
- (47) Perdew, J. P.; Burke, K.; Ernzerhof, M. Generalized Gradient Approximation Made Simple. *Phys. Rev. Lett.* **1996**, *77*, 3865.
- (48) Perdew, J. P.; Wang, Y. Pair-Distribution Function and Its Coupling-Constant

1
2
3 Average for the Spin-Polarized Electron Gas. *Phys. Rev. B* **1992**, *46*, 12947.

4
5 (49) Blöchl, P. E. Projector Augmented-Wave Method. *Phys. Rev. B* **1994**, *50*, 17953.

6
7 (50) Monkhorst, H. J.; Pack, J. D. Special Points for Brillouin-Zone Integrations.
8 *Phys. Rev. B* **1976**, *13*, 5188.
9
10
11
12
13
14
15
16
17
18
19
20
21
22
23
24
25
26
27
28
29
30
31
32
33
34
35
36
37
38
39
40
41
42
43
44
45
46
47
48
49
50
51
52
53
54
55
56
57
58
59
60

1
2
3
4
5
6
7
8
9
10
11
12
13
14
15
16
17
18
19
20
21
22
23
24
25
26
27
28
29
30
31
32
33
34
35
36
37
38
39
40
41
42
43
44
45
46
47
48
49
50
51
52
53
54
55
56
57
58
59
60

For Table of Contents Only

